Supporting information

Revealing the disrupted Li/vacancy structure in Co, Mg, and Al co-doped ultra-high Ni-rich cathodes.

Hang Li, [1,2]* Weibo Hua[3], Alexander Missyul[4], Thomas Bergfeldt[2], Michael Knapp[2], Helmut Ehrenberg[2], Feng Pan[1], * and Sylvio Indris[2,5] *

[1]School of Advanced Materials, Peking University, Shenzhen Graduate School, Shenzhen 518055, China. E-Mail: 2206393335@pku.edu.cn; panfeng@pkusz.edu.cn;

[2]Institute of Applied Materials (IAM), Karlsruhe Institute of Technology (KIT), 76344, Eggenstein-Leopoldshafen, Germany. E-Mail: Sylvio.indris@kit.edu;

[3]School of Chemical Engineering and Technology, Xi'an, Shanxi, 710049, China.

[4]CELLS-ALBA, Synchrotron, E-08290 Barcelona, Spain.

[5]Applied Chemistry and Engineering Research Centre of Excellence (ACER CoE), Université Mohammed VI Polytechnique (UM6P), Lot 660, Hay Moulay Rachid, Ben Guerir, 43150, Morocco

Methods

Materials synthesis

First, the co-precipitation method was used to prepare the spherical precursors of $Ni_{0.94}Co_{0.03}Mg_{0.02}Al_{0.01}(OH)_2$, $Ni_{0.97}Co_{0.03}(OH)_2$ and $Ni(OH)_2$. A continuous stirred tank reactor (CSTR) with a capacity of 1.2 L was used under an air atmosphere. 200 mL of deionized water was added to the CSTR and kept at 55 °C. Three kinds of water solutions (denoted as solution A, solution B, and solution C) were used. Solution A (300 mL) was prepared by dissolving $NiSO_4 \cdot 6H_2O$, $CoSO_4 \cdot 7H_2O$, and $MgSO_4$ in deionized water at a designed concentration. Solution B (300 mL) was obtained by mixing $Al_2(SO_4)_3 \cdot 18H_2O$, NaOH (2.0 M), and NH_4OH (2.0 M) in deionized water. The high concentrations of NaOH can turn Al^{3+} into AlO_2^-. Solution C was 3.0 M NaOH. Solution A and solution B were added into the CSTR with the same flow rate simultaneously. The pH of the mixed solution in the CSTR was maintained at 10.7 ± 0.2 by controlling the flow rate of solution C. The stirring speed and temperature of the solution in the CSTR were controlled strictly. The greenish precursor powder was filtered and then washed with deionized water several times until the pH of the filtrate was close to 7.0. The filtered powder was dried at 120 °C overnight.

Second, the dried hydroxide precursor powder is mixed thoroughly with $LiOH \cdot H_2O$ powder with 2% excess (molar ratio) Li as compensation at high temperatures. The mixtures are calcined in a tube furnace at 550 °C for 6 h and then at 700 °C for 12 h under an oxygen flow of 50 mL min^{-1}.

Electrochemical tests

The electrochemical performances are tested in the CR-2025-coin cell. First, the cathode slurry is prepared by uniformly mixing the active material, C65 carbon black, and polyvinylidene fluoride at a mass ratio of 92:4:4. Second, the well-mixed slurry is coated on Al foil with a thickness of 150 μm. The N-methyl pyrrolidone (NMP) solvent was removed by drying the electrode in an oven at 120 °C for 3 h in air. The electrode is cut into discs with a diameter of 12 mm, and the mass loading of active material is 8–9 mg cm^{-2}. Finally, the coin cell is assembled in the Ar glovebox using a Li chip (diameter = 16.7 mm) as a counter electrode and Celgard-2025 as the separator. The electrolyte is 1 M LiPF$_6$ dissolved in ethylene carbonate: ethyl methyl carbonate = 3:7 solvent with 2 wt% vinylene carbonate as an additive. All cells were tested using a VMP3 multichannel potentiostat (Bio-Logic, France) at room temperature (25 °C). The test voltage is 2.8-4.3 V. The impedance tests are performed by a Biologic BCS potentiostat (Bio-Logic, France) from 1MHz to 1 mHz.

X-ray techniques

Synchrotron-based *in situ* XRD experiments were performed at the MSPD beamline at ALBA synchrotron with an energy of 30 keV (λ = 0.4130 Å). The diffraction patterns were acquired using a MYTHEN 2D position-sensitive detector. The exposure time for each pattern was 60 seconds. CR2025 coin cells with glass windows (diameter = 5 mm) were used.[1] The experiments of determining the crystallographic structure of the pristine materials were conducted at the MS beamline of Paul Scherrer Institute (PSI), Villigen, Switzerland, and the P02.1 beamline of PETRA-III, DESY, Hamberg, Germany.[2] Synchrotron-based X-ray absorption (XAS) experiments were carried out at the P65 beamline of PETRA-

III. The XAS data were collected at the Ni K-edge (8333 eV) in fluorescence mode. X-ray absorption near-edge structure (XANES) spectra were obtained by subtracting the pre-edge background from the overall absorption and normalizing it with a spline fit using the ATHENA software package.[3]

Solid-state nuclear magnetic resonance (NMR) spectroscopy

All NMR experiments were conducted on a Bruker Avance 200 MHz spectrometer at a magnetic field of 4.7 T. For the ^{6}Li magic-angle spinning (MAS) NMR experiments, the spectra were acquired with 1.3 mm rotors at a spinning speed of 60 kHz. The recycle delay was set to 1 s and the Larmor frequency was 29.5 MHz. ^{6}Li MAS NMR spectra were measured using a rotor-synchronized Hahn-echo pulse sequence (90°-τ-180°-τ-acquisition) with a 90° pulse length of 1.6 μs. The ^{6}Li NMR shifts were referenced using an aqueous 1 M ^{6}LiCl solution (0 ppm). All spectra were normalized for sample mass and number of scans. For the *ex situ* ^{6}Li NMR measurement, the electrodes were charged to certain states of charge (SoC). When cycling was finished, the cathodes were taken out of the disassembled cells, washed with dimethyl carbonate (DMC) three times, and dried naturally in the glovebox for 24 hours. The electrodes were then scraped from the Al current collectors and filled into the 1.3 mm diameter NMR rotors.

Elemental Analysis

The Li, Ni, Co, Mn, Mg, and O content of the samples was determined via inductively coupled plasma-optical emission spectroscopy (ICP-OES) using a Thermo Fischer Scientific iCAP 7600 DUO. The mass fraction was determined from three independent measurements. About 10 mg of the samples were dissolved in 6 mL of hydrochloric acid and 2 mL of nitric acid at 353 K for 4 h in a graphite

oven. The digestions were diluted, and analysis of the elements was accomplished with four different calibration solutions and an internal standard (Sc). The range of the calibration solutions did not exceed a decade. Two or three wavelengths of elements were used for calculation. The O content was analyzed by carrier gas hot extraction (CGHE) using a commercial oxygen/nitrogen analyzer TC600 (LECO). The O concentration was calibrated with the certified standard KED 1025, a steel powder from ALPHA. The standards and samples were weighed with a mass in the range from 1 - 2 mg together with 5 mg of graphite in Sn crucibles (9 - 10 mm) and wrapped. Together with a Sn pellet, the wrapped samples were put into a Ni crucible and loaded in an outgassed (6300 W) double-graphite crucible. The measurements took place at 5800 W. The evolving gases, CO_2 and CO, were swept out by He as inert carrier gases and measured by infrared detectors.
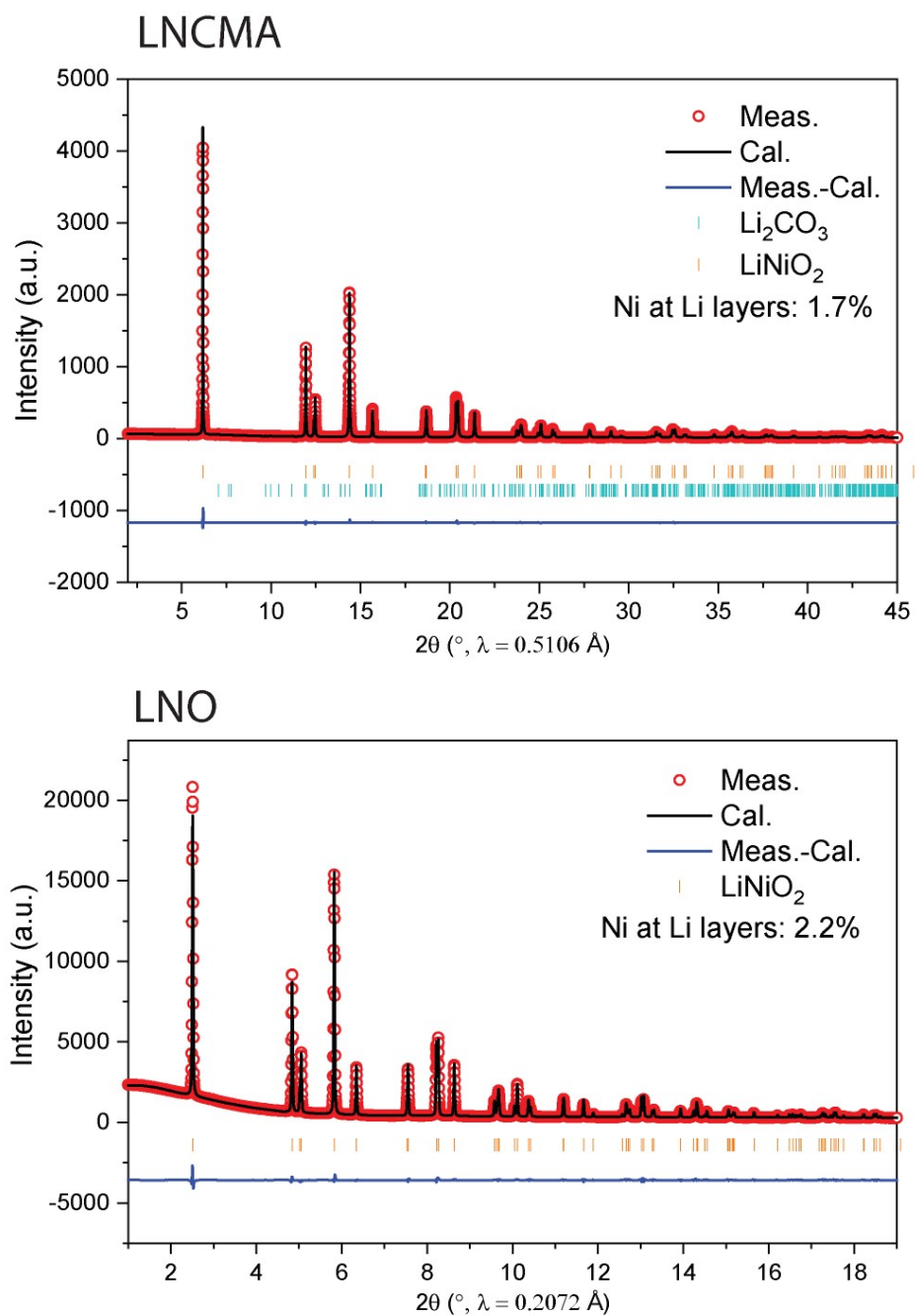
**Figure S1.** Rietveld refinement of LNCMA and LNO against synchrotron-based XRD patterns.
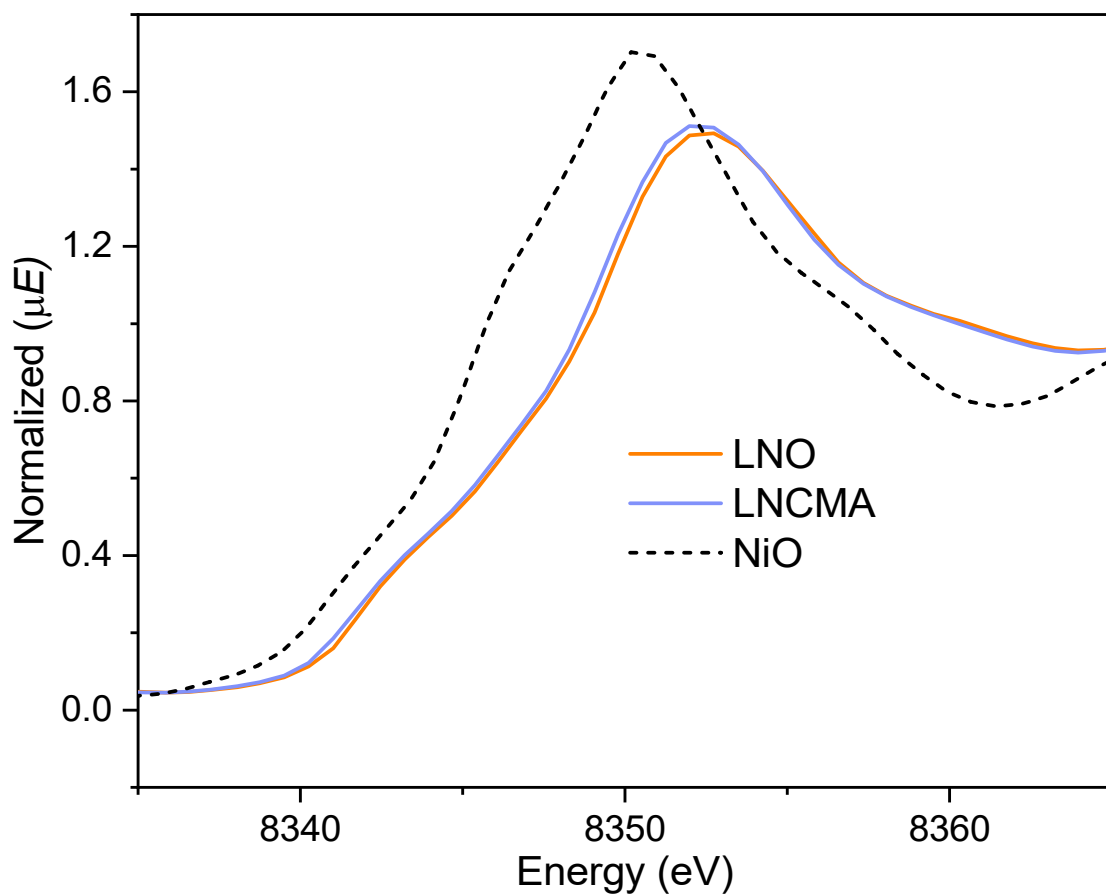
Figure S2. Ni K-edge XANES spectra of the LNO and LNCMA. NiO was also measured as a reference sample.
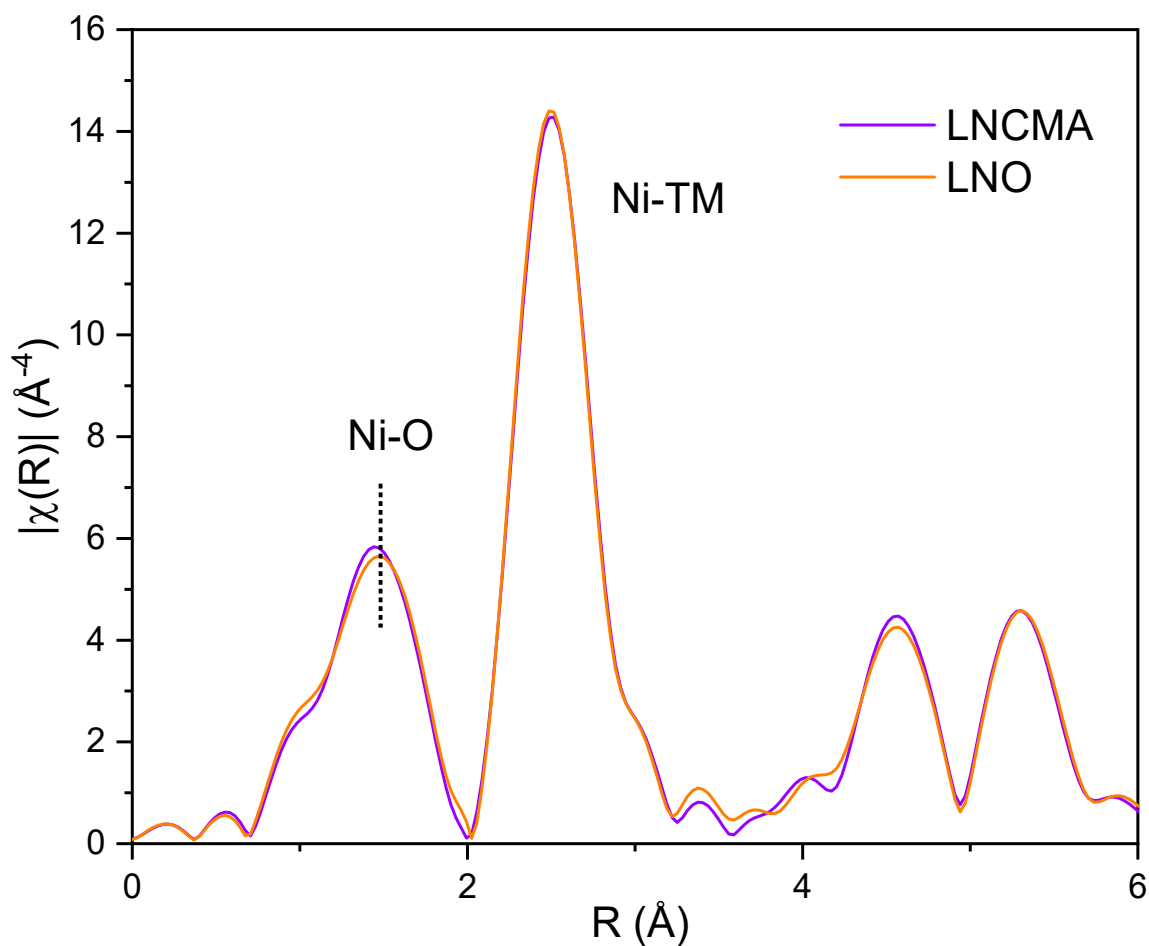
Figure S3. FT-EXAFS spectra for Ni K-edge of the LNO and LNCMA. The EXAFS spectra for Ni show two distinct peaks between 1.0 and 3.5 Å. The first peak at 1.5 Å corresponds to the Ni-O scattering interaction and LNCMA exhibits a slightly shorter Ni-O distance compared to that of LNO, in line with the decreased Ni-O bond length after co-doping in LNO. The second peak at about 2.5 Å corresponds to the Ni-TM interaction and no obvious difference in peak position is obtained between the two spectra.
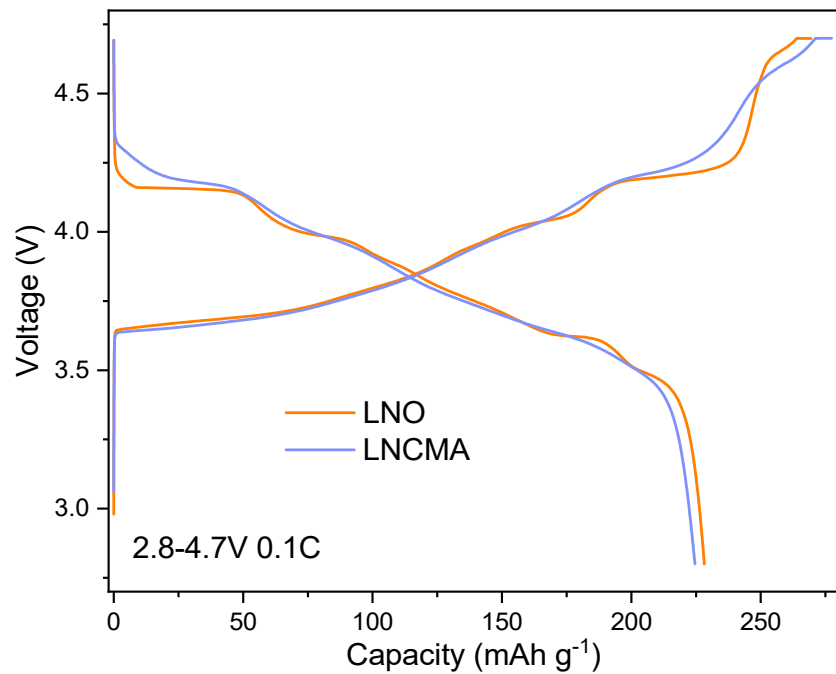
Figure S4. The voltage-capacity profiles of *in situ* cells in the synchrotron XRD experiments.
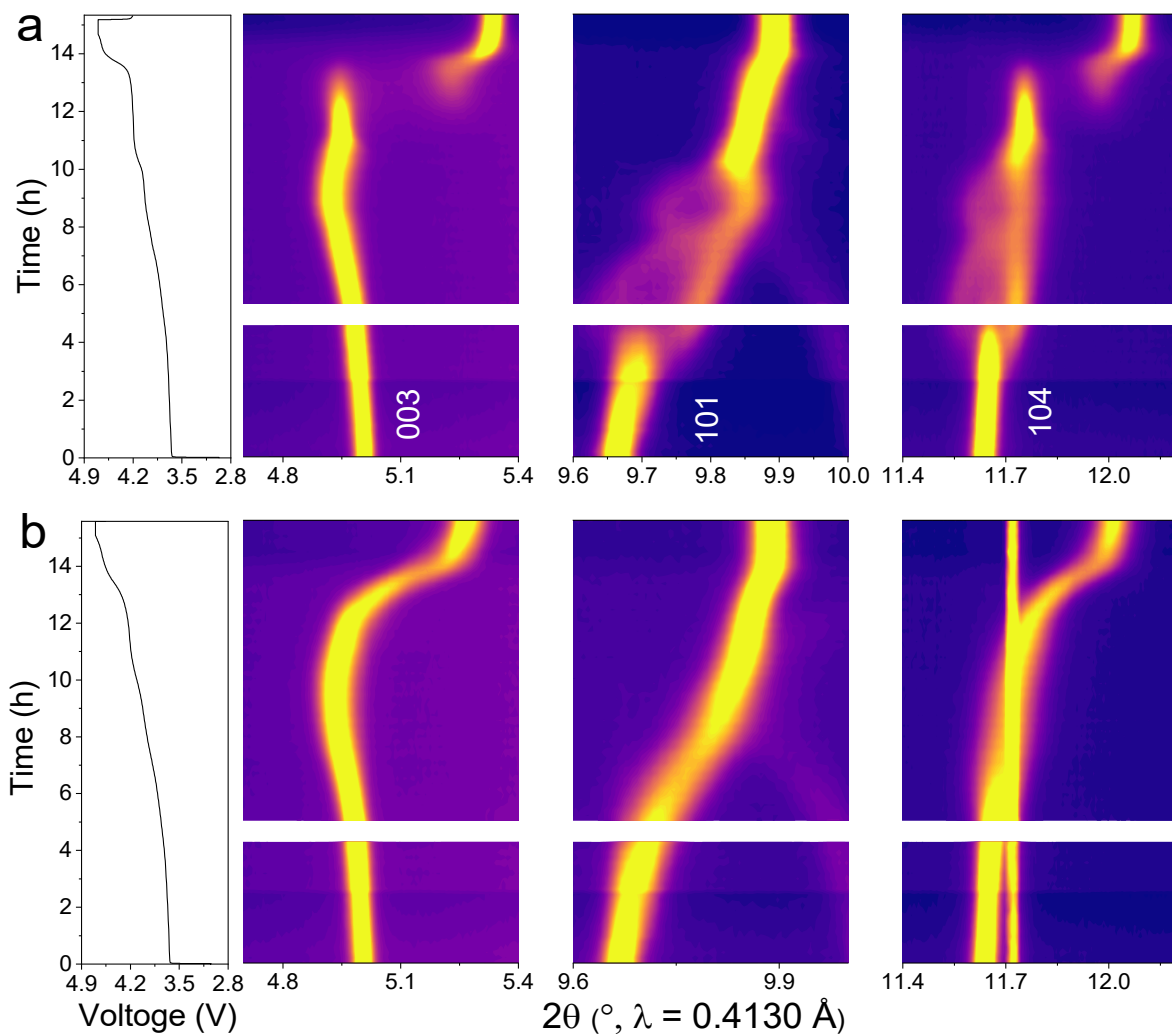
Figure S5. Contour plots of synchrotron-based *in situ* XRD patterns at selected 2θ ranges with the corresponding charge curves for **a**. LNO, and **b**. LNCMA. Regarding LNO, the original 101 reflection gradually disappeared and two new reflections, $20\bar{1}$ and 110 increased in intensity, which could be assigned to the monoclinic phase. The same peak splitting can also be observed for the 104 reflection, where $20\bar{2}$ and 111 reflections gradually replace the original single reflection. In contrast, no obvious peal splitting associated with the H1 to M transition could be observed upon charge for LNCMA, indicating the distortion in the basal plane was effectively suppressed.
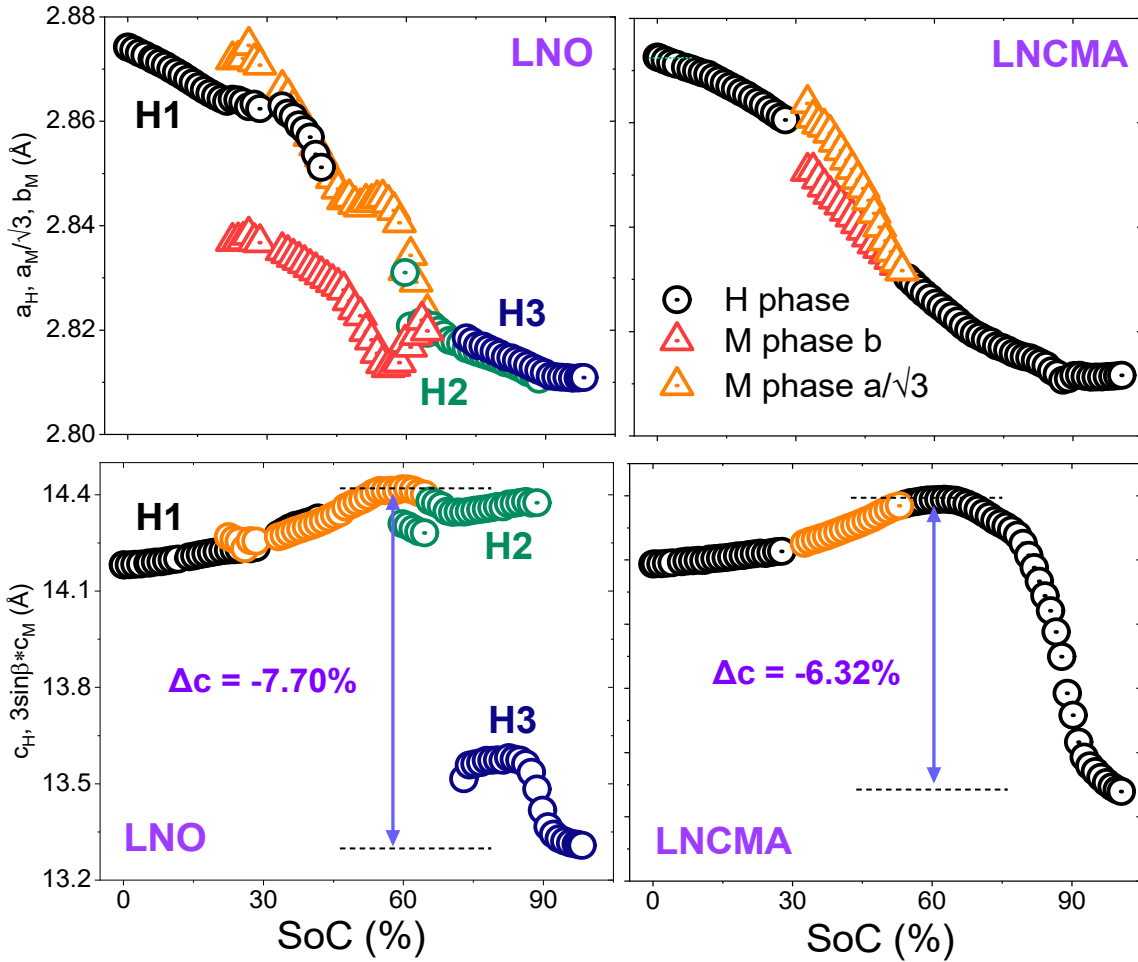
Figure S6. Corresponding changes of lattice parameters during the *in situ* XRD experiments. The lattice contraction/collapse in the *c* direction has been alleviated after co-doping. The decrease of the *c*-lattice parameter changes from 7.70% for LNO to 3.32% for LNCMA. The lattice parameters a_M, b_M, and c_M of the M phase were transformed into hexagonal lattice parameters a_H and c_H, using the relationships as $b_M=a_H$, $a_M=\sqrt{3}a_H$, and $c_M=\sin\beta \cdot c_H/3$.[4] The transformed lattice parameters are plotted together with the hexagonal lattice parameters. Regarding the *a*-axis lattice parameter, if there is no distortion in the monoclinic phase, $a_M/\sqrt{3}$ should be equal to b_M and the distortion extent can be evaluated by comparing these two lattice parameters. As displayed, the LNO cathode experienced a large distortion in the basal plane, supported by the large separation in the two lattice parameters. In comparison, the deviation considerably decreased in the LNCMA cathode.
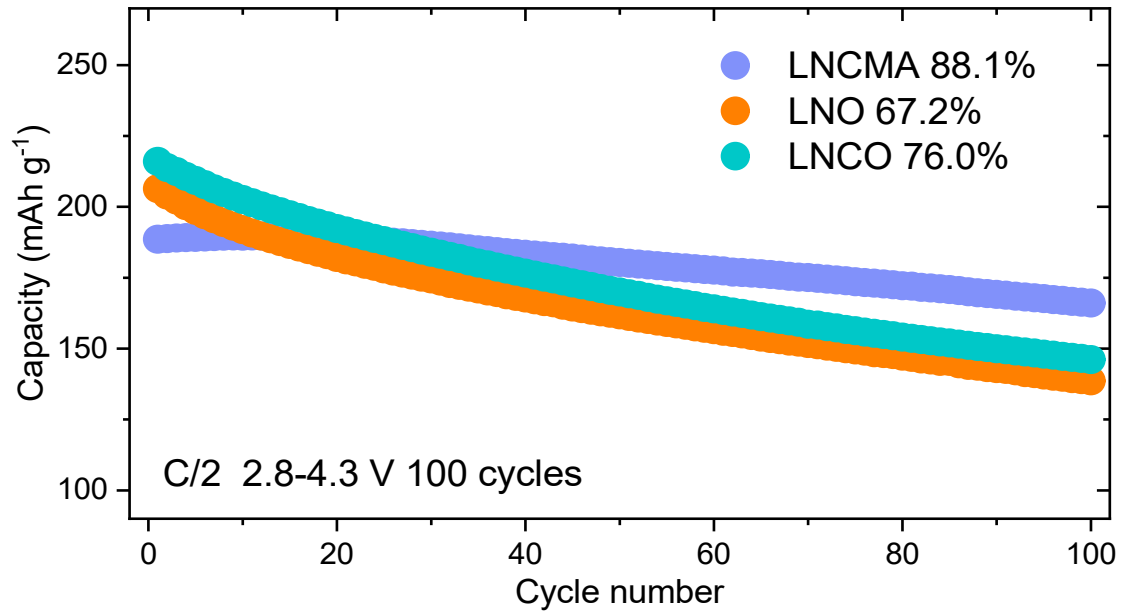
Figure S7. The cycling performance of LNO, LNCO and LNCMA cathodes with the cycling conditions written in the image.
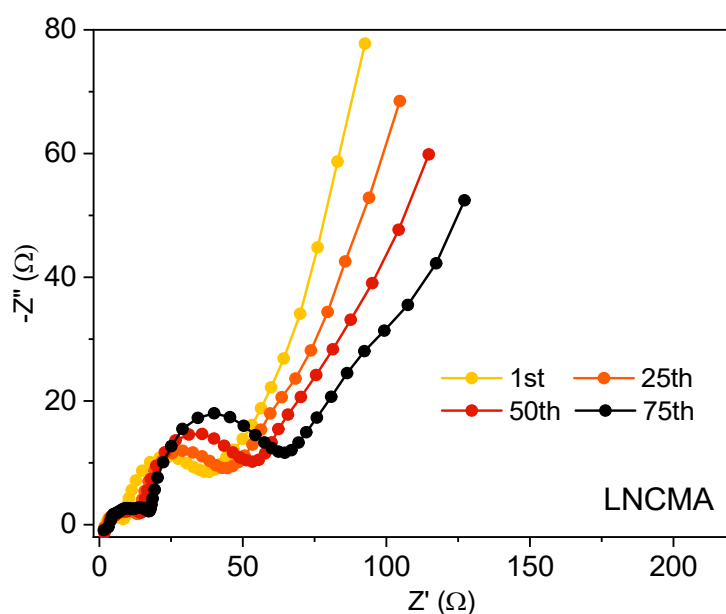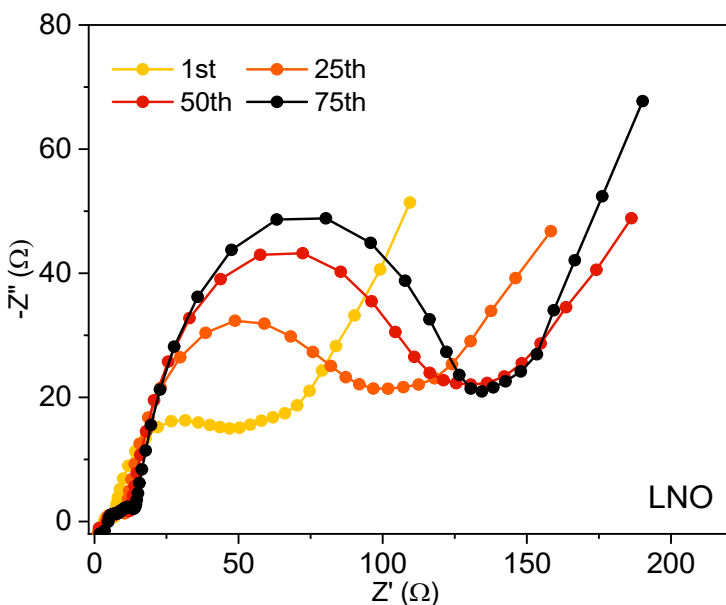
Figure S8. Nyquist plots of the LNO and LNCMA cathodes. The data were obtained for the cells charged at 4.3V at the 1st, 25th, 50th, and 75th cycles after three formation cycles. The charge transfer resistance, R_{ct}, is estimated from the second semicircle at medium-low frequency. The R_{ct} of the LNCMA was initially 30.5Ω, which gradually increased to 33.8Ω after 50 cycles, and finally to 41.1Ω after 75 cycles. For the LNO cathode, the initial charge transfer resistance was similar in magnitude at 36.3Ω. However, the R_{ct} increased dramatically to 87.8Ω after 50 cycles and to 109.5Ω after 75 cycles. The impedance data suggests that the surface degradation process between the cathode and the electrolyte is mitigated owing to

the suppressed phase transitions, especially the H2 to H3 transition at high voltage regions. The LNO cathodes suffer from severe electrode-electrolyte reactions due to phase transition-induced particle cracking and the high reactivity of Ni^{4+} upon cycling.[7]
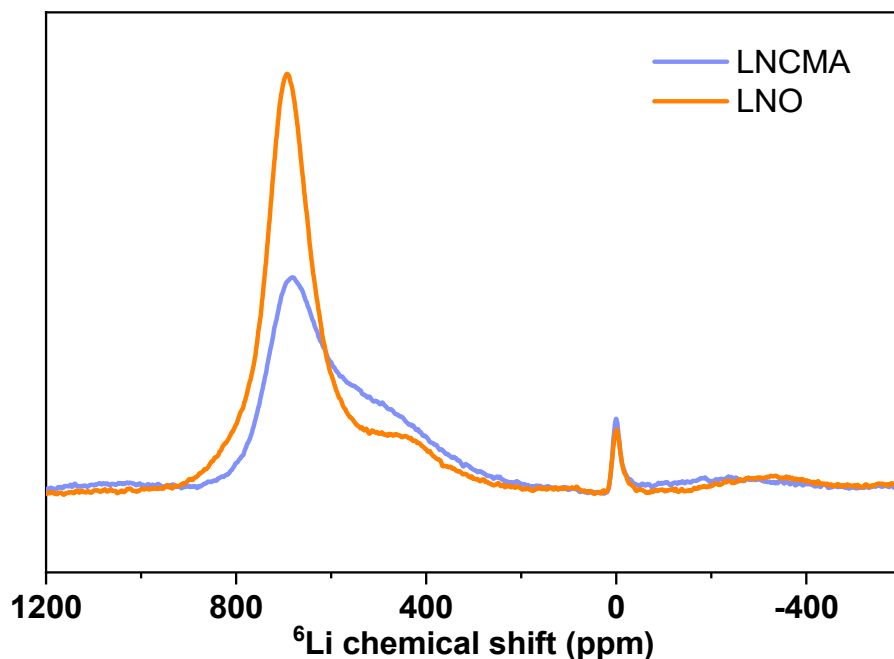
Figure S9. The ^6Li NMR spectra of the LNO and LNCMA in the pristine states. For LNO, there is an NMR signal located at 450 ppm, which could be assigned as the Li in the Ni layers or Li in the twin boundaries.[5,6] Regarding LNCMA, there are more intense contributions on the right-hand side of the main peak compared to that of LNO. It could be rationalized by the appearance of the new environment, in which paramagnetic Ni ions are substituted by diamagnetic dopants (Co, Mg, and Al) in the coordination sphere of lithium ions. In all spectra, there are sharp signals at around 0 ppm, which stem from some minor diamagnetic components, for example, Li_2CO_3.
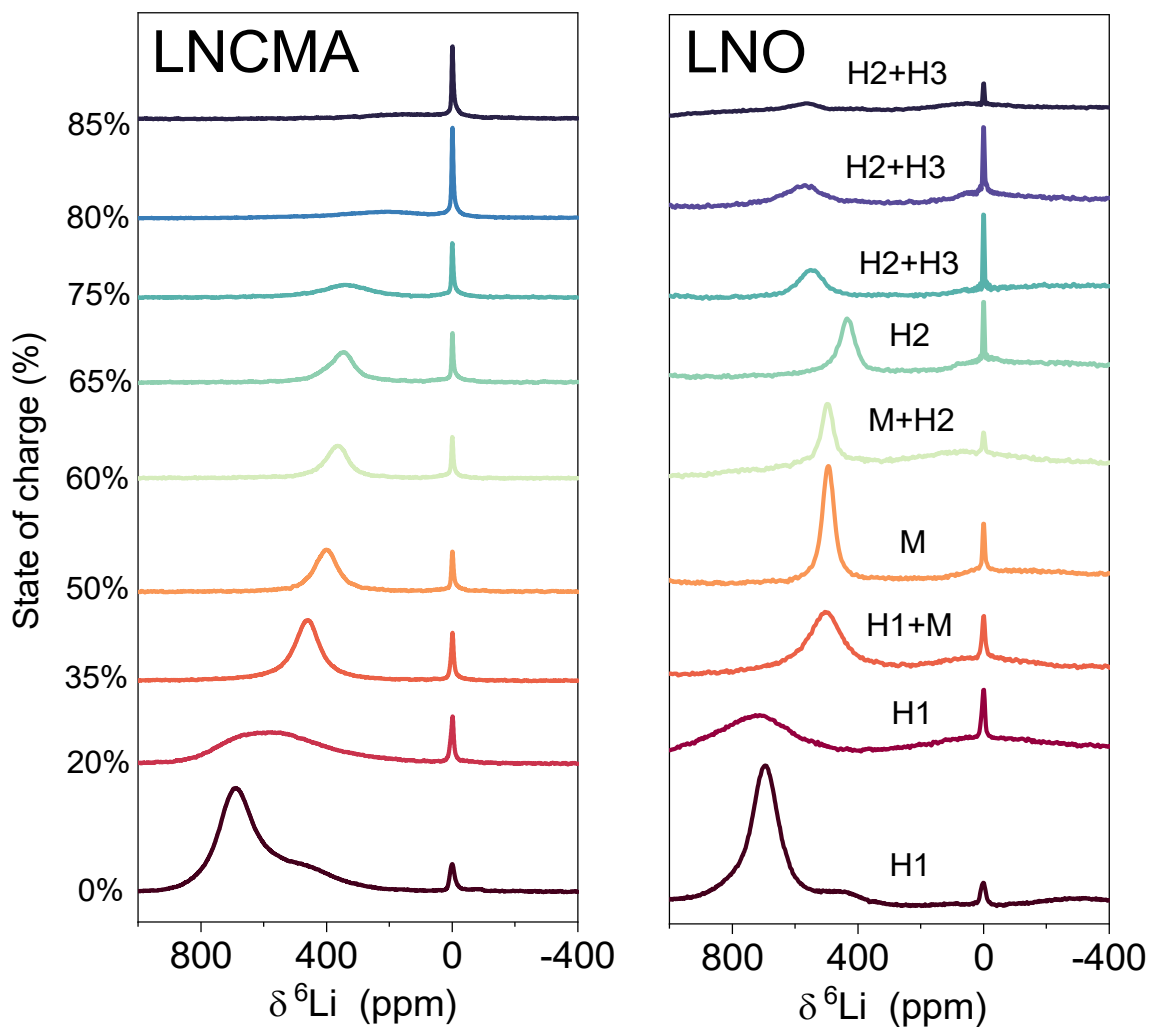
Figure S10. *Ex situ* NMR spectra of LNO and LNCMA cathodes with different states of charge. For each NMR spectrum of LNO, the corresponding phase composition is also provided based on the input from the *in situ* XRD.
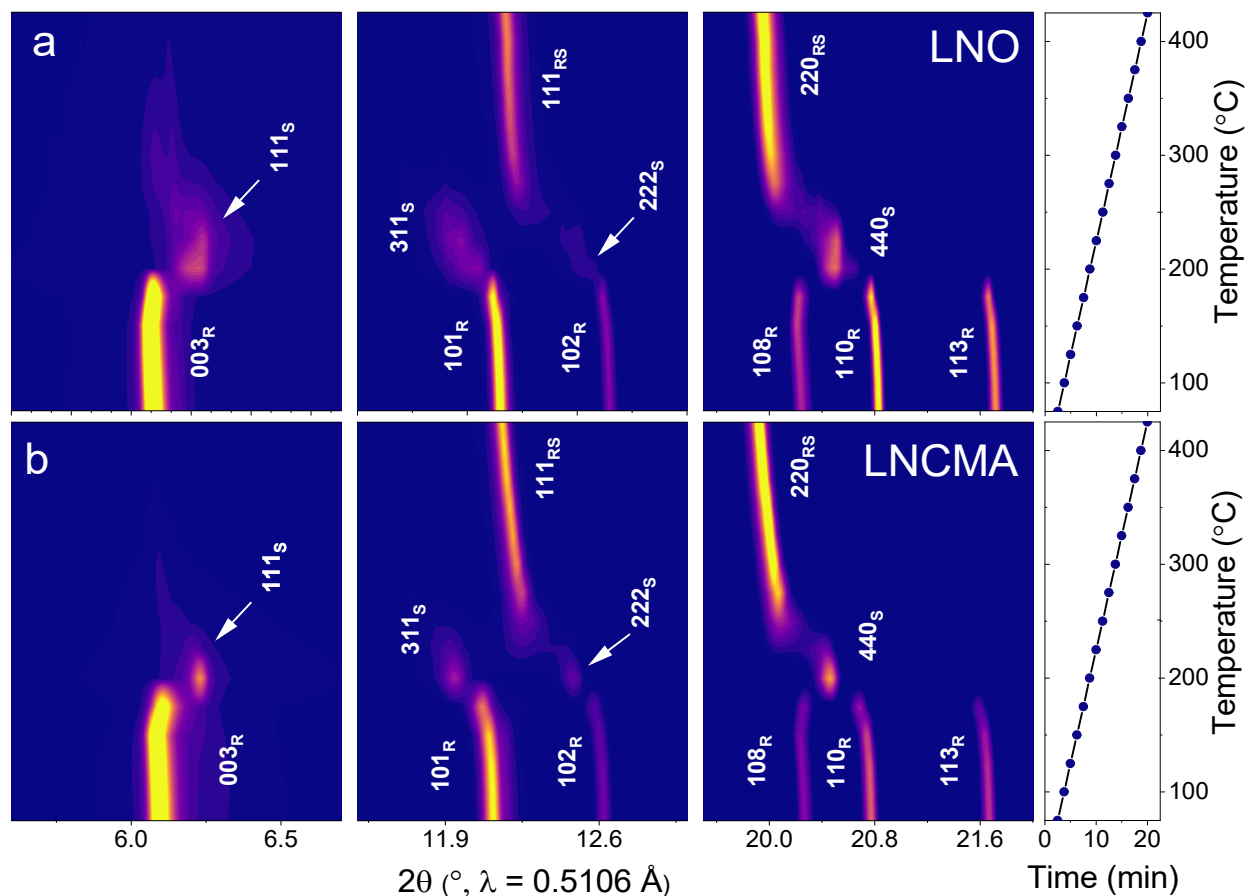
Figure S11. Synchrotron-based *in situ* heating XRD experiments of LNO (a) and LNCMA (b) are used to investigate the irreversible phase transition route during thermal decomposition. The image above displays a series of *in situ* XRD patterns of the charged LNO and LNCMA electrodes at 4.3 V that were collected continuously while heating up to 500°C without the electrolyte. The layered structure transforms to a spinel structure for both cathodes, indicated by the full disappearance of the 003_R reflection and the appearance of a series of new reflections (111_S, 311_S, 440_S…). As the temperature is further increased, the rock-salt phase appears, as revealed by the gradually increasing intensities of the 111_{RS} and 220_{RS} peaks with rising temperature. Two charged electrodes exhibit similar thermal behaviors, indicating that a small number of dopants could not induce a comparatively profound effect on the thermal stability as their effect on the phase transition behavior as well as the cycling stability. The thermal decomposition of Ni-rich materials is mainly driven by the oxygen release and the fast reduction of Ni from Ni^{4+} to Ni^{2+}. These two processes are less sensitive to the dopants inside the lattice structure.

Note 1
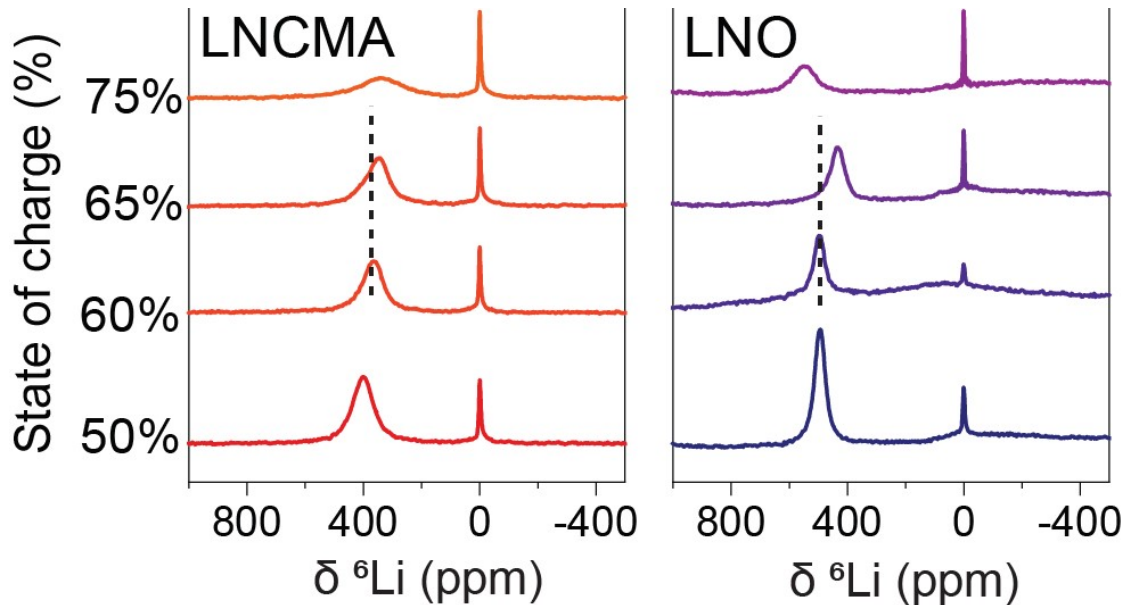
As shown above, there is a right NMR shift in the spectra for both materials when the SoC is increased from 60% to 65%. However, a much larger shift is obtained for LNO. This can be rationalized by the influence of the phase transitions. As shown in **Fig. S10**, at SoC60%, the phase transition from the monoclinic phase (M) to the second hexagonal phase (H2) just started, with only 7% H2 phase being formed. At SoC65%, the phase transition has been completed with the pure H2 phase being formed. Since the M phase is formed by certain distortions from the hexagonal phase, there is a large difference in bond length and bond angles. Those differences influence the orbital overlapping and electron delocalization, thus further moving the NMR signal to lower ppm positions. Regarding LNCMA, there is no obvious monoclinic distortion during the charging period, so the signal moving is mostly only influenced by the oxidation of Ni^{3+}. That single influencing factor causes the limited right shift of the NMR signal.
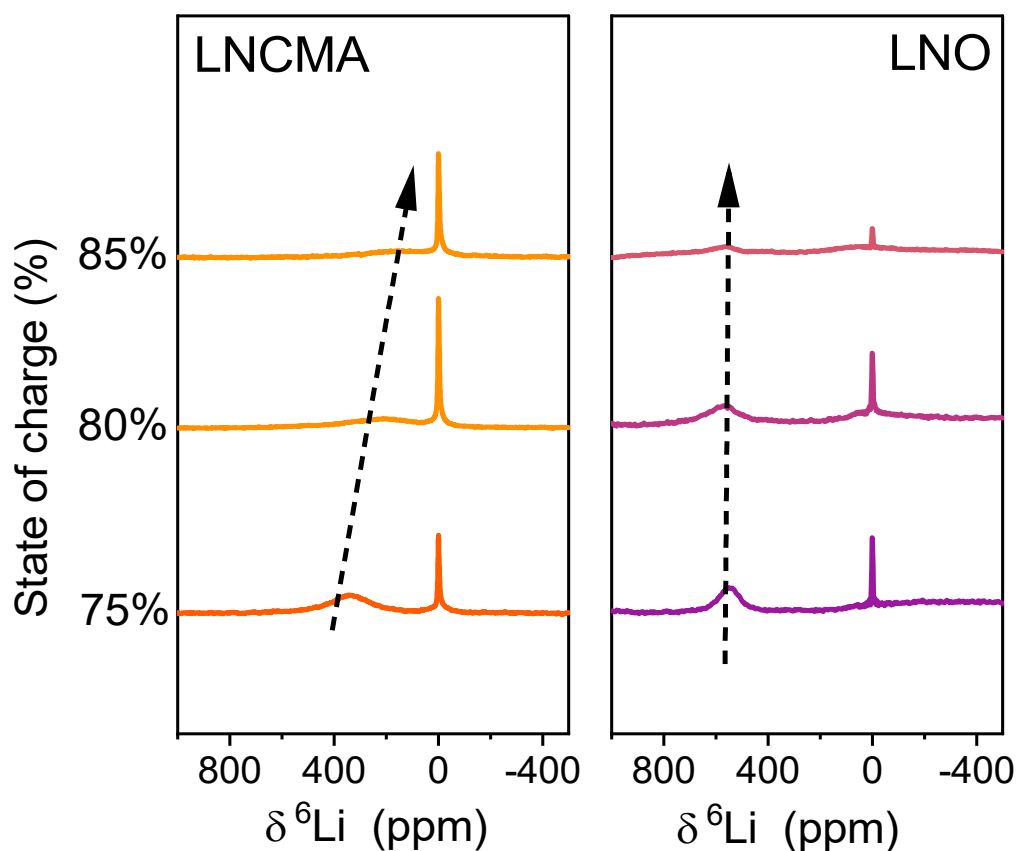
The increase in the NMR signal mostly happens between SoC65% and SoC75%. The NMR signal hardly moves in the region from SoC75% to SoC85%. This can be rationalized by the corresponding situations of phase transitions (see **Fig. S10**): the phase transition from H2 to H3 starts between SoC65% and SoC75% and continues until the end state, i.e. SoC85%. Such a phase transition undergoes a two-phase manner, where Li is continuously removed from the H2 phase to form the H3 phase. In the bulk material, the relative content of H2 keeps decreasing and the content of H3 increases oppositely. The NMR signal that appears at around 548 ppm corresponds to the Li local environments in the H2 phase and the decrease in the signal intensity is just in line with the decreased content of the H2 phase. The NMR signal of the H3 phase should appear close to the position of 0 ppm (overlapped with the signal from Li salts) because most of the Ni is oxidized to Ni^{4+}.

Note 2

The dopants can be placed either in the full-filled Ni rows or in the empty Ni rows in the ordering structure of $Li_{0.5}NiO_2$, as displayed below. When dopants are located at empty Ni rows, the Li anchored by dopants has to be placed in the empty Li rows (denoted by Li with orange colors) because as discussed by J.R. Dahn, these Li atoms are placed in a vertex-sharing site with dopants (a 180° dopant-O-Li bond).[9] In such an assumption, Li in full-filled Li rows has the same Li local environment as that of LNO SoC50%. There are six 180° Ni-O-Li interactions and two 90° Ni-O-Li interactions, giving rise to an NMR shift of 630 ppm. If so, the chemical shift of LNCMA would be the same as the one of LNO at SoC 50%. The pinned Li would have four 90° Ni-O-Li interactions, resulting in a chemical shift of -60 ppm. However, no signal has been observed in the negative region in the spectrum. Therefore, the assumption of such an arrangement of dopants is out of our consideration. In contrast, when dopants are placed in the full-filled Ni rows, they will decrease the average number of 180° Ni-O-Li interactions from six to five, and all Li (free-moving Li and anchored Li) has the same coordination environment: two 90° Ni-O-Li bonds and five 180° Ni-O-Li bonds. That would induce a chemical shift of 520 ppm, in line with the experimental values.
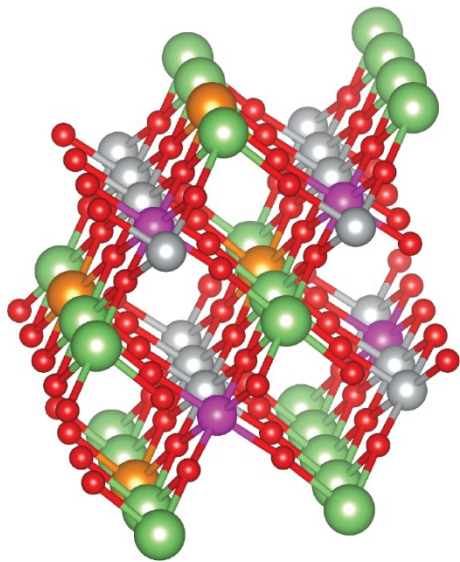
dopants in filled Ni rows   dopants in empty Ni rows

🟢 Li ⚪ Ni 🟣 Co/Mg/Al 🟠 anchored Li 🔴 O
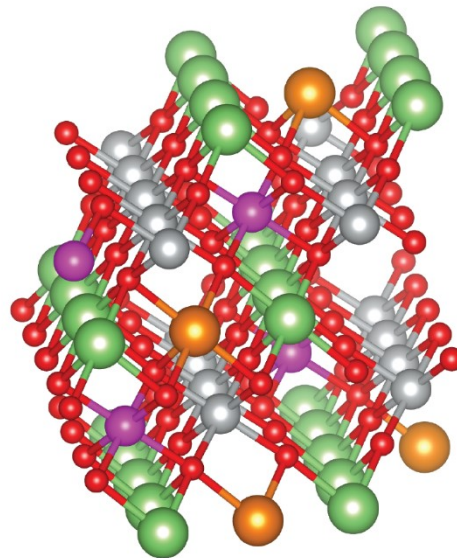
Table S1. ICP-OES results of LNCMA.

	Li	Ni	Co	Mg	Al	O
LNCMA	1.066	0.940	0.030	0.020	0.010	2.164

Table S2. Crystallographic data of LNO determined from the XRD Rietveld refinement results.

LNO	χ^2 = 2.1, Bragg R-factor 3.51				
Space group $R\bar{3}m$ a = 2.87671(4) Å, c = 14.19532(34) Å V = 101.735(3)					
Atom	Site	x/a	y/b	z/c	Occupancy
O	6c	0	0	0.25810(37)	1.000
Li	3b	0	0	0.5	0.978(4)
Ni2	3b	0	0	0.5	0.022(4)
Ni1	3a	0	0	0	1.000
Bond lengths: Ni-O 1.9746(10)Å Li-O 2.1079(12) Å					
Ni-O-Li bond angle (1): 174.73(9)° bond angle (2): 90.095(6)°					

Table S3. Crystallographic data of LNCMA determined from the XRD Rietveld refinement results.

LNCMA	χ^2 = 8.1, Bragg R-factor 7.80				
Space group $R\bar{3}m$ a = 2.87751(9) Å, c = 14.19635(71) Å V = 101.798(6)					
Atom	Site	x/a	y/b	z/c	Occupancy
O	6c	0	0	0.26009(78)	1.000
Li	3b	0	0	0.5	0.912(7)
Ni2	3b	0	0	0.5	0.017(7)
Ni1	3a	0	0	0	1.000
Co	3a	0	0	0	0.030
Al	3a	0	0	0	0.020
Mg	3a	0	0	0	0.010
Bond lengths: Ni-O 1.9599(10)Å Li-O 2.1258(11) Å					
Ni-O-Li bond angle (1): 173.44(8)° bond angle (2): 89.987(7)°					

References

1. Herklotz, M. *et al.* A novel high-throughput setup for *in situ* powder diffraction on coin cell batteries. *J. Appl. Crystallogr.* **49**, 340–345 (2016).

2. Willmott, P. R. *et al.* The Materials Science beamline upgrade at the Swiss Light Source. *J. Synchrotron Radiat.* **20**, 667–682 (2013).

3. Ravel, B. & Newville, M. ATHENA, ARTEMIS, HEPHAESTUS. Data analysis for X-ray absorption spectroscopy using IFEFFIT. *J. Synchrotron Radiat.* **12**, 537–541 (2005).

4. H. Li, N. Zhang, J. Li, J. R. Dahn. Updating the Structure and Electrochemistry of Li_xNiO_2 for $0 \leq x \leq 1$. *J. Electrochem. Soc.* **165**, A2985 (2018).

5. A. R. Genreith-Schriever, C. S. Coates, K. Märker, I. D. Seymour, E. N. Bassey, C. P. Grey. Probing Jahn–Teller Distortions and Antisite Defects in $LiNiO_2$ with ^7Li NMR Spectroscopy and Density Functional Theory. *Chem. Mater.*, **36**, 4226 (2024).

6. H. Nguyen, R. Silverstein, A. Zaveri, W. Cui, P. Kurzhals, S. Sicolo, M. Bianchini, K. Seidel, R. J. Clément. Twin Boundaries Contribute to The First Cycle Irreversibility of $LiNiO_2$. *Adv. Funct. Mater.* 2306168 (2023).

7. C. S. Yoon, D. W. Jun, S. T. Myung, Y. K. Sun. Structural Stability of $LiNiO_2$ Cycled above 4.2V. *ACS Energy Lett.* **2**, 1150 (2017).

8. K. W. Nam, S. M. Bak, E. Hu, X. Yu, Y. Zhou, X. Wang, L. Wu, Y. Zhu, K. Y. Chung, X. Q. Yang. Combining In Situ Synchrotron X-Ray Diffraction and Absorption Techniques with Transmission Electron Microscopy to Study the Origin of Thermal Instability in Overcharged Cathode Materials for Lithium-Ion Batteries. *Adv. Funct. Mater.*, **23**, 1047 (2013).

9. Li, H.; Cormier, M.; Zhang, N.; Inglis, J.; Li, J.; Dahn, J. R. Is Cobalt Needed in Ni-Rich Positive Electrode Materials for Lithium Ion Batteries? *J. Electrochem. Soc.* **166**, A429–A439 (2019).